Combining satellite observations and reanalysis energy transports to estimate global net surface energy fluxes 1985-2012

Article

Accepted Version

It is advisable to refer to the publisher's version if you intend to cite from the work. See Guidance on citing.

www.reading.ac.uk/centaur

CentAUR

Central Archive at the University of Reading

Reading's research outputs online

Combining satellite observations and reanalysis energy transports to estimate global net surface energy fluxes 1985-2012

Chunlei Liu[1], Richard P. Allan[1,2,3], Paul Berrisford[3,4], Michael Mayer[5], Patrick Hyder[6], Norman Loeb[7], Doug Smith[6], Pier-Luigi Vidale[1,3] and John M. Edwards[6]

[1] *Department of Meteorology, University of Reading, Reading, UK*

[2] *National Centre for Earth Observation, UK*

[3] *National Centre for Atmospheric Science, UK*

[4] *ECMWF, Shinfield Park, Reading, UK*

[5] *Department of Meteorology and Geophysics, University of Vienna, Austria.*

[6] *Met Office, Exeter, UK*

[7] *NASA Langley Research Centre, Hampton, Virginia, USA*

ABSTRACT

Two methods are developed to estimate net surface energy fluxes based upon satellite-based reconstructions of radiative fluxes at the top of atmosphere and the atmospheric energy tendencies and transports from the ERA-Interim reanalysis. Method 1 applies the mass adjusted energy divergence from ERA-Interim while method 2 estimates energy divergence based upon the net energy difference at the top of atmosphere and the surface from ERA-Interim. To optimise the surface flux and its variability over ocean, the divergences over land are constrained to match the monthly area mean surface net energy flux variability derived from a simple relationship between the surface net energy flux and the surface temperature change. The energy divergences over the oceans are then adjusted to remove an unphysical residual global mean atmospheric energy divergence. The estimated net surface energy fluxes are compared with other data sets from reanalysis and atmospheric model simulations. The spatial correlation coefficients of multi-annual means between the estimations made here and other data sets are all around 0.9. There are good agreements in area mean anomaly variability over the global ocean, but discrepancies in the trend over the eastern Pacific are apparent.

Introduction

The absolute mean value of net radiation imbalance at the top of atmosphere (TOA) is a key climate variable, providing an estimate of total energy gain of the Earth system and a link between radiative forcing, ocean heat uptake and surface temperature response. It has been estimated to be 0.5 to 1 W/m^2 for the global mean in recent studies [*Hansen et al.*, 2011; *Loeb et al.*, 2012; *Trenberth et al.*, 2014; *Wild et al.,* 2015] using changes in total ocean heat content (OHC) [*Lyman and Johnson*, 2014; *Trenberth et al.,* 2014; *Smith et al.,* 2015; *Roemmich et al.,* 2015] and making assumptions about minor energy sinks including the land, the atmosphere and the cryosphere. Although satellite data provide regional coverage of top of atmosphere radiative fluxes, the net surface fluxes display

much larger uncertainty due to the lack of constraints from global observations [*Trenberth et al.*, 2009; *Wild et al.*, 2013; *Wild et al.*, 2015].

The net energy fluxes at the earth's surface, including short and long-wave radiation and the sensible and latent heat fluxes, are very important for the study of surface temperature change, and the atmospheric and oceanic circulations. The surface fluxes also control the water cycle since the incoming short wave radiation provides much of the energy required for surface water evaporation. Net downward surface energy can accumulate within the ocean, leading to long time-scale effects on the climate. Therefore accurate estimation of the surface energy fluxes is essential for understanding both the short term temperature hiatus [*Easterling and Werner,* 2009; *Knight et al.,* 2009; *Trenberth and Fasullo*, 2013a; *Huber and Knutti*, 2014; *Watanabe et al.,* 2014] and long term climate change [*Otto et al*., 2013]. It is difficult to obtain accurate absolute surface fluxes from satellites due to complicated atmospheric conditions affecting the retrieval processes in particular relating to the numerous surface variables required by turbulent flux bulk formulae [*Schmetz*, 1991].

The net input of radiation fluxes at TOA are modulated by the atmosphere and re-distributed by lateral energy transports [*Keith, 1995; Chiodo and Haimberger*, 2010; *Lucarini and Ragone*, 2011; *Trenberth and Fasullo*, 2013a; *Mayer and Haimberger*, 2012; *Mayer et al.,* 2014; *England et al.,* 2014; *Loeb et al.*, 2015]. *Meehl et al.* [2011] and *Trenberth and Fasullo* [2013b] also demonstrated that the vertical energy redistribution in the oceans is likely to have contributed substantially to the slowing in the rate of global average surface temperature increase in the last fifteen years. Assessment of where the net accumulation of energy in the climate system is being stored within ocean basins [*Balmaseda et al.,* 2013*; Drijfhout et al.*, 2014; *Llovel et al.*, 2014; *Desbruyères et al*., 2014; *Roemmich et al.,* 2015] is required for understanding the mechanisms of energy redistribution associated with internal variability and therefore the surface temperature variations.

The currently available surface flux data sets have some limitations. Observed data from in situ measurements are sparsely distributed in space, while satellite-derived retrievals contain substantial uncertainties and require further validation. Observationally-based data, reanalysis estimates and climate model simulations show a large spread in the data and large unrealistic global imbalances when turbulent and radiative flux products are combined [*Trenberth et al.*, 2009; *Stephens et al.,* 2012; *Wild et al.,* 2013]. In this study, we apply an atmospheric energy divergence approach [*Chiodo and Haimberger*, 2010; *Mayer and Haimberger*, 2012] using two different methods to estimate the net downward surface energy fluxes by combining reconstructed net radiation fluxes at TOA [*Allan et al.,* 2014] with the energy tendencies and lateral divergence simulated by the ERA-Interim reanalysis [*Dee et al.,* 2011; *Berrisford et al.,* 2011].

Data and methods

2.1 Data sets

The key data set is the ECMWF (European Centre for Medium-Range Weather Forecasts) ERA-Interim reanalysis (ERAINT) [*Dee et al.,* 2011]. Various observational data are assimilated to a weather forecast model to provide representations of atmospheric states. Although it has some known problems, such as the lack of volcanic aerosols and the omission of the 11 year solar cycle [*Dee et al.,* 2011], it provides a comprehensive representation of atmospheric variables and estimates of energy divergences and fluxes required for this study. The net radiation flux at TOA is based on the recent reconstruction by *Allan et al.* [2014] using satellite observations from the Clouds and the Earth's Radiant Energy System (CERES; *Loeb et al.,* 2012) and Earth Radiation Budget Satellite (ERBS) wide field of view (WFOV, 72 day mean) non-scanning instrument [*Wong et al.*, 2006],

ERA-Interim reanalysis and climate model simulations applying the Atmospheric Modelling Intercomparison Project 5 (AMIP5) experimental setup with prescribed observed sea surface temperature (SST) and sea ice and realistic radiation forcings [*Taylor et al.,* 2012]. The net TOA flux is adjusted to ensure agreement with an observational estimate over the period 2005-2010, primarily determined by observed 0-2000m ocean heating rate [*Loeb et al.,* 2012; *Allan et al.,* 2014]. The TOA reconstructions are updated using the latest version (version 2.8) of CERES data. Another important update from *Allan et al.* [2014] is that prior to March 2000, reconstructed radiative fluxes are adjusted separately for each hemisphere rather than applying a global adjustment. This adjustment ensures that deseasonalized anomalies in radiative fluxes match the WFOV variability for 0-60°S and 0-60°N regions. Further details of the additional adjustment procedures are described in *Allan et al.* [2014]. The updated net downward TOA radiation flux will be referenced as F_T.

Sixteen AMIP5 models are used in this study and one member from each model is chosen. Data from a 5 member ensemble of the UPSCALE (UK on PRACE - weather-resolving Simulations of Climate for globAL Environmental risk) [*Mizielinski et al.*, 2014] simulations are also used here. UPSCALE is from a global atmospheric model (HadGEM3-A-GA3; *Walters et al.* [2011]) at 25km resolution, which is employed to produce an extended AMIP simulation up to 2011 using the Operational Sea Surface Temperature and Sea Ice daily high resolution Analysis (OSTIA, *Donlon et al.* [2012]). The only differences between these 5 ensemble member runs are their initial conditions: each member was perturbed by randomly altering the lowest order bit in the 3D potential temperature field.

The recently available ECMWF 20th century atmospheric reanalysis from ERA-CLIM (European Reanalysis of Global Climate Observations) project (hereafter ERA20C) is used here for comparison purpose; it is a single member reanalysis and it assimilates observations of surface pressure and surface marine winds; SST, sea ice and realistic radiative forcings are prescribed [*Poli et al.,* 2013]. The atmospheric energy divergence from the MERRA (Modern Era-Retrospective Analysis for Research and Applications) reanalysis is also used for the comparison of net surface energy fluxes. A large quantity of observational data are assimilated in the MERRA system using a three-dimensional variational data assimilation analysis algorithm [*Rienecker et al.,* 2011]. Observed surface temperature data are from HadCRUT4 [*Morice et al.,* 2012]. All data used in this study are monthly mean diagnostics accumulated from higher time resolution data and are listed in Table 1.

2.2 Methods

2.2.1 Surface energy flux from mass adjusted divergence

Following *Berrisford et al*. [2011], the total energy (*E*) in an atmospheric column can be written as

$$E = \frac{1}{g}\int_0^1 (Lq + C_p T + \varphi_s + k)\ \frac{\partial p}{\partial \eta} d\eta \tag{1}$$

where L, q, C_p, T, φ_s and k are the latent heat of condensation of water, specific humidity, the specific heat capacity of air at constant pressure, temperature, surface geopotential and kinetic energy ($(\boldsymbol{V} \cdot \boldsymbol{V})/2$; $\boldsymbol{V}$ is the horizontal wind velocity vector), respectively. p is the pressure, g is the gravitational acceleration and η is the hybrid vertical coordinate which is a function of pressure and surface pressure [*Simmons and Burridge,* 1981]. The total energy tendency $\frac{\partial E}{\partial t}$ in each atmospheric column can be expressed as

$$122 \qquad \frac{\partial E}{\partial t} = -\nabla \cdot \frac{1}{g} \int_0^1 \mathbf{V}(h+k)\, \frac{\partial p}{\partial \eta}\, d\eta + F_A \qquad\qquad (2)$$

123 The total energy input to the atmosphere $F_A = F_T - F_S$ where F_T is the net downward radiation flux
124 (difference between the absorbed solar radiation and the outgoing longwave radiation) at TOA and
125 F_S is the net downward energy flux including contributions from both radiation flux and turbulent
126 heat fluxes at surface. The moist static energy $h = Lq + C_p T + \varphi$ (φ is geopotential). Note, a further
127 term could be added to the right hand side of (2), to represent a budget residual, which in reanalysis
128 data would be due to analysis increments and numerical effects. Rearranging (2) allows F_S to be
129 obtained from

$$130 \qquad F_S = F_T - \frac{\partial E}{\partial t} - \nabla \cdot \frac{1}{g}\int_0^1 \mathbf{V}(h+k)\, \frac{\partial p}{\partial \eta}\, d\eta \qquad\qquad (3).$$

131 The total energy tendency, $\frac{\partial E}{\partial t}$, is small compared with other terms and can be calculated from time

132 series of E computed from ERA-Interim analyses while $\nabla \cdot \frac{1}{g}\int_0^1 \mathbf{V}(h+k)\, \frac{\partial p}{\partial \eta}\, d\eta$ is the energy

133 divergence (E_D). The horizontal flux in E_D is not simply the flux of total energy from equation (1),
134 but incorporates the flux of enthalpy [*Boer,* 1982; *Trenberth and Solomon*, 1994).

135

136   For mass consistency, the output E_D from ERA-Interim should be mass adjusted, because during
137 the assimilation procedure, observations reset the surface pressure field, whereas the mass fluxes are
138 not adjusted accordingly [*Graversen et al.,* 2007; *Berrisford et al*. 2011]. Based on *Mayer and*
139 *Haimberger* [2012],

$$140 \qquad E_{Dmass} = E_D - (\bar{h} + \bar{k})(M_{DIV} + M_{TEND} + P - E_{vap}) \qquad\qquad (4),$$

141 where M_{DIV} and M_{TEND} are vertically integrated total mass divergence and tendency obtained from
142 the ERA-Interim reanalyses. The difference between evaporation (E_{vap}) and precipitation (P) is
143 calculated from total column water vapour (w) content based on the method of *Trenberth et al.*
144 [2001],

$$145 \qquad E_{vap} - P = \frac{\partial w}{\partial t} + \nabla \cdot \frac{1}{g}\int_0^1 q\mathbf{V}\, \frac{\partial p}{\partial \eta}\, d\eta = w_{TEND} + w_{DIV} \qquad\qquad (5),$$

146 where w_{DIV} is vertically integrated water vapour divergence and w_{TEND} is total column water vapour
147 tendency which can be calculated from the time series of total column water vapour content. Both are
148 obtained from ERA Interim; this method is considered more accurate than using $E_{vap} - P$ directly
149 from the reanalysis, since water vapor is assimilated, but precipitation is a simulated variable that is
150 highly dependent upon model parameterisations. It includes water mass transfer due to phase change
151 between water vapour and liquid water. The phase change between liquid water and ice in the
152 atmosphere has been ignored and the horizontal water transport due to cloud advection is also
153 neglected since these terms are small, $\bar{h}$ and $\bar{k}$ are the vertical average of moist static energy and
154 kinetic energy, respectively, which can be computed from analysed ERA-Interim fields.

155

156 From equation (3), we can have the net surface energy flux from the mass adjusted energy
157 divergence (F_{mass}):

158 $$F_{mass} = F_T - \frac{\partial E}{\partial t} - E_{Dmass} \qquad (6).$$

159

160 Similar procedures are applied to MERRA data [*Mayer et al.*, 2013] to obtain mass adjusted total
161 energy divergence $E_{Dmass-MERRA}$ which is substituted into equation (6) to obtain the net downward
162 surface flux $F_{mass-MERRA}$.

163

164 *2.2.2 Surface energy flux from model residual divergence*

165 Another way to estimate the atmosphere energy divergence is to calculate it directly from ERA-
166 Interim as a residual of energy fluxes [*Chiodo and Haimberger*, 2010; *Mayer and Haimberger*,
167 2012]:

168 $$E_{Dres} = F_{T-ERA} - F_{S-ERA} - \left(\frac{\partial E}{\partial t}\right)_{fc} \qquad (7),$$

169 where F_{T-ERA} and F_{S-ERA} are energy fluxes at the TOA and surface computed directly from the
170 ERA-Interim 12-hourly forecasts, where their radiation components (shortwave and longwave) are
171 calculated from the radiation transfer model based on the atmospheric states. F_{S-ERA} also includes
172 turbulent fluxes simulated by the reanalysis. The term $\left(\frac{\partial E}{\partial t}\right)_{fc}$ is mass corrected forecasted total
173 energy tendency [*Mayer and Haimberger*, 2012] and is preferred over analysed tendencies to be
174 consistent with forecasted TOA and surface fluxes. The calculated E_{Dres} can be used to estimate the
175 surface flux (F_{res}) using the reconstructed TOA flux and total energy tendency from ERA-Interim
176 analyses.

177

178 $$F_{res} = F_T - \frac{\partial E}{\partial t} - E_{Dres}$$

179 $$= F_{S-ERA} + (F_T - F_{T-ERA}) + \left(\frac{\partial E}{\partial t}\right)_{fc} - \frac{\partial E}{\partial t} \qquad (8)$$

180

181 The accuracy of this divergence relies on the accuracy of the atmospheric properties, the radiative
182 transfer through the atmosphere and the turbulent energy calculations at the surface. It is known that
183 ERA-Interim does not represent aerosol forcing due to volcanic eruptions, most notably following
184 the Mt. Pinatubo eruption [*Allan et al.*, 2014], which might affect the divergence (E_{Dres}) accuracy
185 since the radiation fluxes are affected by aerosols. Although the constraint on divergence is poor,
186 hence the need for mass adjustment, data assimilation constrains parameters towards an observed
187 atmospheric state; with the inclusion of analysis increment, $\left(\frac{\partial E}{\partial t}\right)_{fc} - \frac{\partial E}{\partial t},$ the effect of aerosol-
188 related biases on F_{res} will be reduced.

189

190 **2.3 Adjustment constraints**

191   Since a large quantity of observational data are assimilated into ERA-Interim, it is expected both
192   E_{Dmass} and E_{Dres} will provide reasonable spatial structures, but the E_{Dres} has a multi-annual (2001-
193   2005) global mean value of -0.9 Wm^{-2} which is not physically reasonable since it is expected the
194   global averaged E_D should be zero to guarantee energy conservation. This is because atmospheric
195   models don't, in general, have a closed budget for the atmospheric energy, as a result of inconsistent
196   treatment of turbulent cascades of kinetic energy and water mass [*Lucarini and Ragone*, 2011;
197   *Previdi and Liepert*, 2012; *Lucarini et al*., 2014]. Even though the global mean E_{Dmass} is close to
198   zero (~10^{-4}), the net surface flux derived from it has unrealistically large local changes (2001-2008
199   mean minus 1986-2000 mean, not shown here) and the global mean RMS (root mean square) of the
200   multi-annual mean differences (2001-2008 mean minus 1986-2000 mean) is about 8.5 Wm^{-2}. The
201   area mean E_{Dmass} over land is also large (about 2 Wm^{-2} over 2001-2005). A strategy was required to
202   address these problems. The schematic diagram shown in Fig. 1 illustrates the energy flow terms
203   used in the estimation of net surface energy fluxes. The left and right columns depict the energy flow
204   over land and ocean respectively and there is a net energy transport from the ocean column to land
205   column [*Wild et al*., 2015]. The steps for estimating the monthly net surface energy fluxes are as
206   follows:

207   Remove the global mean divergence from E_{Dmass}.
208   We already have F_T and $\frac{\partial E}{\partial t}$, assuming we have the correct monthly net surface energy flux
209   data over land, the monthly vertically integrated energy divergence can be calculated over
210   land using energy balance equation;
211   The globe is divided into 15° latitude band (30° over Antarctic). The mean discrepancy
212   between mass corrected divergence and the one derived from step (2) over land is
213   redistributed evenly over ocean grid points to keep the total divergence unchanged across
214   each band.
215   The monthly net surface energy flux over the ocean can then be calculated using bias
216   corrected divergence.

217

218   In step (2), it will be ideal to use net surface energy flux calculated from E_{Dmass} as the initial
219   estimation over land, but as mentioned above the derived fluxes have unrealistically large regional
220   changes (2001-2008 mean minus 1986-2000 mean) over land, so the surface energy flux from ERA-
221   Interim (F_{S-ERA}) over land is used as the initial estimation. In order to correct the unrealistic trend
222   and large anomaly variability of F_{S-ERA} as discussed in section 3.3 (which would imply large
223   unrealistic temperature variations or land heat capacity), a simple method described in the next
224   section is applied to estimate the monthly net energy flux variability based on the observationally
225   constrained surface temperature changes over land.

226

2.4 Net energy flux over land

228   The mean global land flux is estimated using the simple relationship of $F_S = C\frac{\Delta T}{\Delta t} + \varepsilon$, where C is
229   the effective mean surface land heat capacity, $\frac{\Delta T}{\Delta t}$ is the global land mean surface temperature change
230   rate and ε is a constant indicating the energy flux penetrating beneath the surface layer. Data from
231   five UPSCALE ensemble members are used for this estimation. The land surface model in
232   UPSCALE simulations is JULES (Joint UK Land Environment Simulator) which has an explicit

representation of the surface energy balance for vegetation, capturing the weaker coupling that exists
between the canopy and underlying soil [*Best et al.,* 2011]. The effective land heat capacity depends
on the soil and canopy properties and the soil water content. After testing we found high correlations
between energy flux and the rate of surface temperature change if $\frac{\Delta T}{\Delta t}$ is calculated from consecutive
months, e.g. the climatology of F_S in April will correlate well with $\frac{\Delta T}{\Delta t}$ calculated from the
climatology difference between April and March, so the effective land heat capacity C and the
constant ε are calculated by regression using the climatology of F_S and climatological $\frac{\Delta T}{\Delta t}$. The
anomaly time series from modeled and reconstructed (from C, $\frac{\Delta T}{\Delta t}$, and ε) land surface mean fluxes
are plotted in Fig. S1. The correlation coefficients (**r**) between monthly anomalies (reference period
2001-2005) are all above 0.6. The plotted lines are 6 month running means and the inflated
reconstructed lines (red) are multiplied by the ratio of the standard deviation between modeled and
reconstructed monthly flux anomalies (values in red in the plot). The variability in F_S is generally
well captured although there are exceptions, notably over the Mt. Pinatubo eruption period since the
constant seasonal C is used while in reality it should vary under anomalous situations; as discovered
by *Iles and Hegerl* [2014], the models underestimate the precipitation over Pinatubo eruption period
which affects the soil moisture content, therefore affecting the relations between temperature change
and energy fluxes. Another factor affecting the net surface energy flux variability is the snow and ice
melting. While there are considerable limitations, this method was applied to ensure that large biases
in the variability in F_S over land did not diminish the realism of diagnosed F_S over ocean which is the
goal of the present study.

Five sets of the regression coefficients from five UPSCALE members using the above method are
applied to the global land mean surface temperature (skin temperature) rate of change $\frac{\Delta T}{\Delta t}$ from
ERA-Interim to get five proxies of mean surface flux; the ensemble mean is used as our estimated
global land mean surface net energy flux. Based on *Beltrami et al.* [2002], the mean net energy flux
over the continental lithosphere is 0.0391W/m^2 over 1950-2000, where the mean land surface
temperature change from HadCRUT4 [*Morice et al.,* 2012] is about 0.0138K/year (from regression).
Based upon the 1985-2012 mean surface temperature change of 0.0298K/year from HadCRUT4 we
estimate the mean of the reconstructed net surface flux as 0.08W/m^2 over this period. Setting this
flux to zero is also reasonable [*Trenberth et al.*, 2009]. Combining algorithms in sections 2.3 and 2.4,
the estimated 2D net surface energy fluxes over land maintains the spatial structure of F_{S-ERA}, but
the monthly area weighted mean values match those from the simple model ($F_{SFC} = C\frac{\Delta T}{\Delta t} + \varepsilon$) and
the long term mean (1985-2012) is anchored to 0.08W/m^2.

3. Net downward energy fluxes

3.1 Net radiation flux at TOA

The reconstructed net downward radiation flux anomalies at TOA are updated from *Allan et al.*
[2014] using the latest version (version 2.8) of CERES data and adjusting pre-CERES variability to
match the interannual anomalies from the WFOV instrument for each hemisphere separately rather
than using the 60ºS-60ºN near-global mean. The TOA flux anomaly time series are plotted in Fig. 2
for the global mean, the global ocean and the global land, respectively. The reference period is from
2001-2005, but WFOV has a reference period of 1985-1999 and is adjusted, for clarity, to match the

274   mean F_T (reconstruction) anomaly over this period. There is good agreement between variability
275   depicted by F_T and the other data sets over the global ocean and the globe. The correlation
276   coefficients (r) between F_T and ERAINT, UPSCALE or AMIP5 monthly anomaly time series are
277   0.63, 0.60, and 0.58 over the global ocean and 0.64, 0.44, and 0.46 over the land, respectively. All
278   these correlations are significant based on the two-tailed test using Pearson critical values at the level
279   of 5%. The degree of freedom of the time series is calculated by first determining the time interval
280   between effectively independent samples [*Yang and Tung,* 1998] but additionally assuming that
281   periods separated by 12 or more months are independent. Although ERAINT does not represent
282   changes in aerosol emissions, most notably following the Mt. Pinatubo eruption in 1991, the
283   correlation coefficient between F_T and ERAINT is still the highest. This reflects the realistic monthly
284   variability of atmospheric circulation patterns through the extensive assimilation of conventional and
285   satellite data by ERA-Interim.

286   The area weighted multi-annual mean net downward energy fluxes from F_T (Fig. 2d) over 2001-
287   2005 are 0.51, 8.35 and -19.0W/m^2 for the globe, the global ocean and the global land, respectively.
288   The difference is mainly due to the albedo difference between the land and the ocean. The large
289   energy deficit over land should be compensated by the horizontal energy transport from ocean to
290   land [*Mayer and Haimberger,* 2012; *Trenberth and Fasullo*, 2013b].

291

3.2 Net energy flux at the surface

293   The multi-annual mean (2001-2005) net surface energy fluxes from F_{mass} are plotted in Fig. 3a and
294   zonal mean variations from F_{mass}, F_{res}, $F_{mass-MERRA}$, ERAINT, ERA20C, UPSCALE and AMIP5
295   data sets are plotted in Fig. 3b-d. The area-weighted means are displayed in the zonal mean plot. The
296   multi-annual mean for other data sets are in Fig. S2. F_{mass} and $F_{mass-MERRA}$ are calculated from the
297   spatially filtered E_{Dmass} and $E_{Dmass-MERRA}$ respectively using a Hoskins spectral filter
298   [*Sardeshmukh and Hoskins,* 1984] with an attenuation of 0.1 at wave number 106 [*Berrisford et al.*,
299   2011]. A filter is necessary due to the noise generated by data assimilation, highlighting that spatial
300   patterns must be interpreted with caution.

301   Despite the contrasting methods and datasets, the multi-annual means for the period 2001-2005 from
302   all data sets show similar spatial structures and zonal means except for the MERRA data which show
303   much stronger fluxes over the central Indian Ocean and central western Pacific. The spatial
304   correlation coefficients of multi-annual means between estimations and other data sets are all around
305   0.9. Over the oceans, despite ~10-20 W/m^2 differences present in the zonal means (Fig. 3c), all
306   datasets capture the positive downward energy flux over the equatorial central and east Pacific areas
307   due to the interaction between the tropical instability waves [*Willett et al.,* 2006] and the equatorial
308   Pacific cold tongue [*Martínez-Garcia et al.,* 2010] controlled by ocean mixing [*Moum et al.,* 2013].
309   The evaporation is less and there is lower outgoing longwave radiation over this cold region
310   compared with surrounding regions. The negative downward fluxes over the Gulf Stream in the
311   North Atlantic and Kuroshio currents in the North Pacific are due to heat and moisture transport from
312   the warm ocean surface to the cold atmosphere above [*Kwon et al.,* 2010]. Over the global land, the
313   UPSCALE simulation has a similar large magnitude residual flux (-0.68W/m^2) to the ERAINT flux
314   (0.71W/m^2) because it does not have a closed energy budget [*Lucarini and Ragone*, 2011]. This is in
315   part because the high resolution version of the UPSCALE simulations used were not re-calibrated
316   using observations since a key aim of this project was to understand the influence of resolution upon
317   mean climate. The unrealistically large magnitude values at around 55 and 65ºS (Fig. 3d) are caused

318 by single grid points at the southern tip of South America and northern tip of the Antarctic peninsula
319 requires further investigation.

320 The mean northward total meridional atmospheric energy transport calculated from E_{Dmass} , E_{Dres}
321 and $E_{Dmass-MERRA}$ are also plotted in Fig. 4a. Peak magnitudes of around 5PW ($1PW = 10^{15}W$) close
322 to 40°S and 40°N are broadly consistent with *Mayer and Haimberger* [2012] and *Lucarini and*
323 *Ragone* [2011] and coincide with the maximum in baroclinic activity [*Lucarini and Ragone,* 2011].
324 The transport from $E_{Dmass-MERRA}$ has stronger magnitude at 40°S/N compared with the other
325 estimates. The transport from E_{Dmass} is of larger magnitude than that from E_{Dres} in the northern and
326 southern hemisphere sub tropics, consistent with *Mayer and Haimberger* [2012].

327 Due to flux constraints over land, the area mean fluxes from both F_{mass} and F_{res} are identical. Their
328 spatial structures and zonal mean variations are also very similar (Fig. 3 and Fig. S2a), but the
329 magnitudes differ in places as shown in Fig. 5a. F_{res} is larger in magnitude than F_{mass} in the south
330 Indian Ocean, but smaller in the north Indian Ocean. F_{res} is smaller over the central, west and north
331 west Pacific, but has larger values over the subtropical gyre of north Pacific, as well as over south
332 east Pacific.

333 Though the mean surface flux spatial structure of ERAINT (Fig. S2b) is similar to the derived ones,
334 its area mean fluxes are unrealistically large over the global ocean (9.30Wm^{-2} in Fig. 3c) compared
335 with ocean observations [*Llovel et al.*, 2014; *Roemmich et al.,* 2015] which are of the order of 0-1
336 W/m^2. ERA-Interim surface fluxes are substantially larger than F_{mass} over the oceans as shown in
337 Fig. 5b, except for the area near the Equator, and this can be seen clearly from the zonal mean
338 variations (Fig. 3c). ERA20C simulates large fluxes into the Southern Ocean, more flux from ocean
339 to atmosphere over the whole Indian Ocean and the north and south Atlantic subtropical gyres (Fig.
340 5c). As stated earlier, the $F_{mass-MERRA}$ (Fig. 5d) has larger values over the central Indian Ocean and
341 central western Pacific, but smaller values over much of the eastern Pacific. UPSCALE shows the
342 common feature of smaller flux over the north Indian Ocean and larger energy flux over the Southern
343 Ocean, but the strong flux over the western Pacific and smaller energy flux over the Eastern Pacific
344 are not apparent in other data sets (Fig. 5e). The ensemble mean from AMIP5 simulations show
345 much lower fluxes into the Western Pacific (Fig. 5f) and this is mainly contributed from CMCC,
346 CNRM, FGOALS, GISS, MRI and INMCM4 model simulations as shown in Fig. S3.

347

3.3 Changes in downward energy flux

349 In order to investigate where the energy is moving through the climate system [*Lucarini and Ragone*,
350 2011; *Mayer and Haimberger*, 2012; *Guemas et al.*, 2013; *Allan et al.,* 2014; *Mayer et al.,* 2014;
351 *Drijfhout et al.*, 2014], considering the changes of multi-annual means in the net downward energy
352 fluxes at both TOA and surface are informative. A preliminary assessment of the multi-annual mean
353 changes (2001-2008 mean minus 1986-2000 mean) from reconstruction (F_T, F_{mass}, F_{res} and
354 $F_{mass-MERRA}$), UPSCALE and AMIP5 data sets are presented in Fig. 6. As discussed by *Allan et al.*
355 [2014], all three data sets show decreased TOA net fluxes over the tropical east Pacific (left column
356 of Fig. 6). The magnitudes of the TOA flux changes over oceans are much smaller than those at the
357 surface.

358 At surface, the estimated changes over land areas are small from estimation (F_{mass} , F_{res} and
359 $F_{mass-MERRA}$), but the flux changes over Russia are slightly larger than in the UPSCALE and AMIP5

360 simulations. Fig. 6b and Fig. 6d show the increasing downward energy flux over the North Pacific
361 and Southern Ocean (increased ocean heat uptake), but negative flux changes over the central
362 Pacific, north Indian ocean and north Atlantic. Although the individual surface flux components are
363 not reconstructed, considering those simulated by ERAINT, the changes appear to be dominated by
364 latent heat fluxes. Comparing with atmospheric model simulations, although both ensemble means
365 from UPSCALE and AMIP5 simulations show decreased fluxes into the central Indian Ocean and
366 north Atlantic (Fig. 6i, l), the big differences are over the Eastern Pacific where simulated increases
367 in downward flux are opposite to the estimations in Fig. 6b,d,f. The estimated surface flux from
368 MERRA ($F_{mass-MERRA}$ in Fig. 6f) is even noisier than those from F_{mass} and F_{res}, but it also displays
369 decreased net downward energy flux over the eastern Pacific. This has been identified as an
370 important region in determining aspects of the recent slowing rate of global surface temperature rise
371 [*Kosaka and Xie*, 2013; *Trenberth and Fasullo*, 2013a; *Meehl et al.,* 2014]. On one hand, the cooling
372 Eastern Pacific will suppress turbulent energy transport from ocean to the atmosphere, so the net
373 downward flux would be increased over this region; on the other hand as demonstrated by *England*
374 *et al.* [2014], the cooling is due to the observed pronounced strengthening in Pacific trade winds
375 which are not represented fully by AMIP simulations. The increased winds will cause more
376 evaporation, so more latent heat transports to the atmosphere. *Brown et al.* [2014] also showed that
377 the surface cooling over Eastern Pacific will enhance the reflected short wave radiation, therefore
378 reduce the net downward energy flux.

379 The eastern tropical Pacific region marked in Fig. 6b,d,f covers 20°N-20°S and 210°E to the west
380 coast of the central America. The mean TOA flux change (2001-2008 mean minus 1986-2000 mean)
381 over this area (Fig. 6a) is -2.1W/m^2 while the surface flux changes from F_{mass} (Fig. 6b) and
382 $F_{mass-MERRA}$ (Fig. 6f) are -3.9W/m^2 and -4.6W/m^2 respectively. Since the total energy tendency is
383 almost zero over this area, the corresponding changes in vertical flux divergence (equal to net surface
384 flux minus net TOA flux; Fig. 6c) over this area are -1.8W/m^2 and -2.5W/m^2 respectively. The
385 negative signs indicate that vertical flux divergence decreased and consequently divergence of
386 horizontal energy transports increased in the 2001-2008 period compared to the 1986-2000 mean
387 (compare equation 6), so both changes in TOA fluxes and atmospheric energy transport contribute
388 roughly equally to the reduced downward surface fluxes over the eastern tropical Pacific from these
389 two mass adjusted data sets. For F_{res} (Fig. 6d) the mean change in surface flux over this area is about
390 -0.5W/m^2 and the corresponding mean change in vertical flux divergence (Fig. 6e) is about 1.6W/m^2
391 which is opposite to the mean changes in vertical flux divergence of F_{mass} and $F_{mass-MERRA}$,
392 implying that increased horizontal energy transport into the east Pacific region offsets much of the
393 reduction in TOA downward fluxes leading to a smaller change in surface fluxes in this case. The net
394 surface flux change obtained from E_{Dres} is weaker than those obtained from E_{Dmass} and
395 $E_{Dmass-MERRA}$, since E_{Dmass} and $E_{Dmass-MERRA}$ are computed from analysed state quantities they
396 are considered more realistic than E_{Dres} which is computed from model forecasts. Changes in TOA
397 fluxes are about -0.5W/m^2 for UPSCALE and AMIP5 data (Fig. 6h,k). The changes at the surface
398 (Fig. 6i,l) are 2.2W/m^2 and 3.3W/m^2 and the corresponding mean divergence changes of horizontal
399 energy transport (Fig. 6j,m) are 2.7W/m^2 and 3.8W/m^2, respectively, implying that increased
400 horizontal energy transport by the atmosphere into the region dominate the simulated changes in the
401 surface fluxes. The divergence difference over the eastern tropical Pacific between the mass adjusted
402 data and those from model simulations requires further study.

403 For the reconstructed surface fluxes (F_{mass} and F_{res}), the global changes from the 1990s to the 2000s
404 (see table S1) are consistent with *Allan et al.* [2014], who considered the TOA net imbalance; there is

an increase in net downward flux at the surface due to the recovery from Pinatubo [*Smith et al.,* 2015]. Consistency with global-mean TOA fluxes is expected since the surface flux estimates are based upon these TOA reconstructions and atmospheric heat capacity is small so cannot uptake a significant fraction of the top of atmosphere imbalance [*Palmer and MacNeal,* 2014]. The ocean heat uptake is also increasing since over 90% of the excess energy into the Earth system is stored in the ocean [*Trenberth and Fasullo,* 2013a]. Consistency between global mean surface and TOA flux changes also applies to ERA20C reanalysis, UPSCALE and AMIP5 simulations (see table S1). *Smith et al.* [2015] highlighted the decline of TOA net downward radiation flux from 1999-2005 which potentially contributed to the recent warming slowdown. Consistent with *Smith et al.* [2015], similar calculations of two five year means centred at 1999 and 2005 from net downward surface energy fluxes show declines of 0.31 Wm^{-2} (reconstruction), 0.51 Wm^{-2} (UPSCALE), 0.07 Wm^{-2} (AMIP5) and 0.26 Wm^{-2} (ERA20C). The differences between flux changes at TOA and surface (Fig. 6h-k) include the total energy tendency and divergence. The patterns are very similar to those surface changes, implies the atmospheric energy divergence is the dominant factor affecting the surface flux changes, since both changes of TOA flux and atmospheric energy tendency are relatively small.

The changes of northward total meridional energy transport calculated from E_{Dmass}, E_{Dres} and $E_{Dmass-MERRA}$ are also plotted in Fig. 4b. Energy transports from mass corrected divergences show the increase of northward transport in the northern hemisphere, but the energy transport from E_{Dres} shows a decrease. It is mixed in the south hemisphere where transport derived from E_{Dres} displays a small energy transport while both calculation from E_{Dmass} and $E_{Dmass-MERRA}$ indicate an increase of poleward energy transport between 10─55ºS and 15─70ºS. The effect of the temporal discontinuities on these changes [*Mayer et al.,* 2013] in the reanalysis, due to artifacts of the observing system, merits further investigation, though the effect is most significant for the partition of the latent and dry static energy and less prominent when considering the total transport [*Trenberth and Fasullo,* 2013b].

The deseasonalised anomaly (calculated relative to the 2001-2005 period) time series of the area weighted mean net downward energy fluxes at the surface from different data sets are plotted in Fig. 7 for the globe, the global ocean and the global land. The time series from both derivations (F_{mass}, F_{res} and $F_{mass-MERRA}$) are identical by design. The light grey shadings are ± 1 standard deviations of the sixteen AMIP5 simulations. All lines are 6 month running means. The ERAINT data are also plotted for reference purpose; spurious trends are explained by latent heat flux changes over the ocean [*Chiodo and Haimberger,* 2010] and from longwave radiation over the land. There is good agreement between derived fluxes and those from AMIP5, ERA20C and UPSCALE data sets over the globe. The correlation coefficients between derived and AMIP5, ERA20C and UPSCALE are 0.38, 0.52 and 0.47, which are significant based on the two-tailed test using Pearson critical values at the level of 5%. Over the global ocean, the coefficients are 0.33, 0.52 and 0.45, which are also statistically significant. Over land the correlation coefficient between derived and ERA20C is 0.60. The correlation coefficients between other data sets can be found in Table S2 and the correlation coefficient maps are in Fig. S4. Future work will consider in more detail the variability across individual ocean basins and comparisons with independent datasets [*Drijfout et al.,* 2014; *Mayer et al.,* 2014; *Desbruyères et al.,* 2014; *Roemmich et al.,* 2015] contributing toward understanding of variation in energy flows into the ocean.

Summary

449 Surface fluxes are a crucial component of the climate system yet global-scale observational estimates
450 are highly uncertain [*Wild et al.,* 2015]. To complement the existing set of surface flux datasets, an
451 alternative method is developed. The net downward energy fluxes at the Earth's surface are
452 estimated through the combination of the reconstructed TOA radiation fluxes [*Allan et al.,* 2014] and
453 the atmospheric energy divergences (Fig. 1) which are calculated using two distinct methods: (1)
454 mass adjusted energy divergence computed from ERA-Interim reanalysis [*Trenberth,* 2001; *Mayer*
455 *and Haimberger*, 2012; *Berrisford et al.,* 2011]; (2) the residual from the difference between the
456 energy fluxes at the TOA and the surface from ERA-Interim.

457 To correct for unrealistic variability in energy fluxes over the land a correction was applied using a
458 simple mean relation between surface flux and surface temperature change in UPSCALE climate
459 model simulations which are strongly dependent upon the model's land surface component, JULES.
460 By setting the global energy divergence to zero, applying the corrected surface fluxes over land and
461 adjusting atmospheric energy divergence from the ocean to the land accordingly the net surface
462 energy flux over ocean could be derived. Although this method relies upon the gross relationship
463 between surface temperature change rate and energy fluxes from a simulation and other assumptions
464 it was found that the sensitivity of the ocean surface flux changes to the methods applied over land
465 are relatively small compared to the differences amongst datasets.

466 The accuracy of the resultant surface fluxes relies heavily on the quality of the reanalysis. The
467 current version of ERA-Interim has some known problems including drifts in energy fluxes and
468 deficient radiative forcing changes relating to anthropogenic and natural aerosol, and problems with
469 mass divergence and conservation [*Berrisford et al.,* 2011]. All these will affect the quality of our
470 product. The assimilation of various observed fields into the model draws towards an observed
471 atmospheric state, so the aerosol effect on the mass adjusted energy divergence (E_{Dmass}) should be
472 less than the effect on E_{Dres}, but the accuracy of the divergence relies on other factors too, such as
473 model spin-up and large time sampling errors, as discussed by *Chiodo and Haimberger* [2010].

474 Different datasets capture the general global patterns of the multi-annual mean net downward surface
475 fluxes despite the contrasting methods involved. The spatial correlation coefficients of multi-annual
476 means (2001-2005) between the reconstruction and other data sets are all around 0.9. The area mean
477 surface flux anomaly time series shows reasonable agreement with AMIP5 (r=0.33), ERA20C
478 (r=0.52) and UPSCALE (r=0.45) simulated monthly anomalies over the global ocean.

479 The change between the 1990s and 2000s over the eastern Pacific differs between datasets: while
480 climate model simulated surface fluxes increase over the period [*Katsman et al.,* 2011], the
481 reconstruction indicates a reduced net downward surface flux. The cooling surface supresses the air-
482 sea turbulent energy exchange, but the strengthening of the observed trade winds [*England et al.,*
483 2014] over this area will reduce the net downward energy flux. Feedbacks involving low-altitude
484 cloud and reflected shortwave radiation may also amplify this response [*Brown et al.,* 2012]. Since
485 the estimated surface fluxes are strongly dependent upon the ERA Interim as well as the MERRA
486 reanalysis which both have temporal homogeneity issues [*Mayer et al.,* 2013], further verification of
487 these products with other data sets from observations, reanalysis and model simulations is required
488 in order to further understand the strengths and weaknesses of the current methodology.

489 Assessing the degree to which SST patterns are driving or being driven by surface flux changes in
490 this region merits investigation [*Mayer et al.,* 2014; *Drijfout et al.,* 2014; *Desbruyres et al.,* 2014].
491 More detailed assessments of recent changes in surface energy fluxes entering distinct ocean basins

492   [*Mayer et al.,* 2014; *Desbruyres et al.,* 2014] will contribute toward improved understanding of
493   energy flows and internal variability in the climate system.

494

495

References

Allan, R. P., C. Liu, N. G. Loeb, M. D. Palmer, M. Roberts, D. Smith, and P.-L. Vidale (2014), Changes in global net radiative imbalance 1985-2012, *Geophys. Res. Lett., 41,* doi:10.1002/2014GL060962.

Arora, V. K., J. F. Scinocca, G. J. Boer, J. R. Christian, K. L. Denman, G. M. Flato, V. V. Kharin, W. G. Lee, and W. J. Merryfield (2011), Carbon emission limits required to satisfy future representative concentration pathways of greenhouse gases, *Geophys. Res. Lett., 38*, L05805, doi:10.1029/2010GL046270.

Balmaseda, M. A., K. E. Trenberth, and E. Källén (2013), Distinctive climate signals in reanalysis of global ocean heat content, *Geophy. Res. Lett*., *40*, 1754–1759, doi:10.1002/grl.50382.

Beltrami, H., J. E. Smerdon, H. N. Pollack, and S. Huang (2002), Continental heat gain in the global climate system, *Geophys. Res. Lett., 29***,** 1167, doi:10.1029/2001GL014310.

Berrisford, P., P. Kållberg, S. Kobayashi, D. Dee, S. Uppala, A. J. Simmons, P. Poli, and H. Sato (2011), Atmospheric conservation properties in ERA-Interim, *Q. J. R. Meteorol. Soc. 137*: 1381–1399, July 2011 B.

Best et al. (2011), The Joint UK Land Environment Simulator (JULES), model description – Part 1: Energy and water fluxes, *Geosci. Model Dev*., *4*, 677–699, doi:10.5194/gmd-4-677-2011.

534 Bi, D., M. Dix, S. Marsland, S. O'Farrell, H. Rashid, P. Uotila, A. Hirst, E. Kowalczyk, M.
535 Golebiewski, A. Sullivan, H. Yan, N. Hannah, C. Franklin, Z. Sun, P. Vohralik, I. Watterson, X.
536 Zhou, R. Fiedler, M. Collier, Y. Ma, J. Noonan, L. Stevens, P. Uhe, H. Zhu, S. Griffies, , and G. J.

537 Boer (1982), Diagnostic Equations in Isobaric Coordinates. *Mon. Wea. Rev.*, *110,* 1801–1820.

538 doi: http://dx.doi.org/10.1175/1520-0493(1982)110<1801:DEIIC>2.0.CO;2.

539

540 Brown, P. T., W. Li, L. Li, and Y. Ming (2014), Top-of-atmosphere radiative contribution to
541 unforced decadal global temperature variability in climate models, *Geophys. Res. Lett., 41*, 5175–
542 5183, doi:10.1002/2014GL060625.

543

544 Chiodo, G., and L. Haimberger (2010), Interannual changes in mass consistent energy budgets from
545 ERA-Interim and satellite data, *J. Geophys. Res., 115*, D02112, doi:10.1029/2009JD012049.

546

547 Collins, W. J., et al. (2011), Development and evaluation of an Earth-system model—HadGEM2,
548 *Geosci. Model Dev. Discuss.*, *4*, 997–1062, doi:10.5194/gmdd-4-997-2011.

549

550 Dee, D. P., et al. (2011), The ERA-Interim reanalysis: Configuration and performance of the data
551 assimilation system, *Q. J. R. Meteorol. Soc*., *137*, 553–597, doi:10.1002/qj.828.

552

553 Delworth, T. L., and Coauthors (2006), GFDL's CM2 global coupled climate models. Part I:
554 Formulation and simulation characteristics. *J. Climate, 19*, 643–674, doi:10.1175/

555 JCLI3629.1.

556

557 Desbruyères, D. G., E. L. McDonagh, B. A. King, F. K. Garry, A. T. Blaker, B. Moat, and H.
558 Mercier (2014), Full-depth temperature trends in the Northeastern Atlantic through the early 21st
559 century, *Geophys. Res. Lett., 41,* 7971-7979, doi: 10.1002/2014GL061844.

560

561 Donlon, C. J., M. Martin, J. Stark, J. Roberts-Jones, E. Fiedler, and W. Wimmer (2012), The
562 Operational Sea Surface Temperature and Sea Ice Analysis (OSTIA) system, *Remote Sens. Environ*.,
563 *116*, 140–158, doi:10.1016/j.rse.2010.10.017.

564

565 Drijfhout, S. S., A. T. Blaker, S. A. Josey, A. J. G. Nurser, B. Sinha, and M. A. Balmaseda (2014),
566 Surface warming hiatus caused by increased heat uptake across multiple ocean basins, *Geophys. Res.*
567 *Lett., 41*, doi:10.1002/2014GL061456.

568

569 Dufresne, J. L., et al. (2013), Climate change projections using the IPSL-CM5 Earth System Model:
570 From CMIP3 to CMIP5, *Clim. Dyn.*, *40*, 2123–2165, doi:10.1007/s00382-012-1636-1.

571

572 Easterling, D. R., and M.F. Wehner (2009), Is the climate warming or cooling? *Geophys. Res. Lett.*
573 *36*, L08706, doi:10.1029/2009GL037810.

574

575 England, M. H., S. McGregor, P. Spence, G. A. Meehl, A. Timmermann, W. Cai, A.S. Gupta,
576 M. J. McPhaden, A. Purich, and A. Santoso (2014), Recent intensification of wind-driven circulation
577 in the Pacific and the ongoing warming hiatus, *Nature Climate Change, 4*, 222-227,
578 doi:10.1038/nclimate2106.

579

580 Gent, P. R., et.al. (2011), The Community Climate System Model version 4. *J. Climate, 24*, 4973–
581 4991, doi: http://dx.doi.org/10.1175/2011JCLI4083.1.

582

583 Guemas, V., F. J. Doblas-Reyes, I. Andreu-Burillo, and M. Asif (2013), Retrospective prediction of
584 the global warming slowdown in the past decade, *Nature Climate Change, 3*, doi:
585 10.1038/nclimate1863.

586

587 Graversen, R. G., E. Källén, M. Tjernström, and H. Körnich (2007), Atmospheric mass-transport
588 inconsistencies in the ERA-40 reanalysis, *Q. J. R. Meteorol. Soc. 133,* 673–680, doi: 10.1002/qj.35.

589

590 Hansen, J., M. Sato, P. Kharecha, and K. von Schuc ann (2011), Earth's energy imbalance and
591 implications, *Atmos. Chem. Phys.*, *11*, 13,421–13,449, doi:10.5194/acp-11-13421-2011.

592

593 Huber, M., and R. Knutti (2014), Natural variability, radiative forcing and climate response in the
594 recent hiatus reconciled, *Nature GeoScience, 7,* doi: 10.1038/NGEO2228.

595

596 Katsman, C. A., and G. J. van Oldenborgh (2011), Tracing the upper ocean's missing heat, *Geophys.*
597 *Res. Lett., 38*(14), L14610, doi:10.1029/2011GL048417.

598

599 Iles, C. E. and G. C. Hegerl (2014), The global precipitation response to volcanic eruptions in the
600 CMIP5 models, *Environ. Res. Lett. 9,* doi:10.1088/1748-9326/9/10/104012.

601

602 Keith, D. W. (1995), Meridional energy transport: uncertainty in zonal means, *Tellus*, *47A*, 30-44.

603

604 Knight, J., J. J. Kennedy, C. Folland, G. Harris, G. S. Jones, M. Palmer, D. Parker, A. Scaife, and P.
605 Stott (2009), Do global temperature trends over the last decade falsify climate predictions? [in "State
606 of the Climate in 2008"]. *Bull. Amer. Meteor. Soc., 90*, S22-S23.

607 Kosaka, Y. and S. P. Xie (2013), Recent global-warming hiatus tied to equatorial Pacific surface
608 cooling, *Nature, 501*, 403–407, doi:10.1038/nature12534.

609 Kwon, Y. O., M. A. Alexander, N. A. Bond, C. Frankignoul, H. Nakamura, B. Qiu, and L. A.
610 Thompson (2010), Role of the Gulf Stream and Kuroshio–Oyashio Systems in Large-Scale
611 Atmosphere–Ocean Interaction: A Review. *J. Climate*, 23, 3249–3281. doi:
612 http://dx.doi.org/10.1175/2010JCLI3343.1.

613 Li, L., et al. (2013), The flexible global ocean-atmosphere-land system model, Grid-point version 2:
614 FGOALS-s2, *Advances in Atmospheric Sciences*, *30,* 543-560, doi: 10.1007/s00376-012-2140-6.

615

616 Llovel, W. J. K. Willis, F. W. Landerer, and I. Fukumoriet (2014), Deep-ocean contribution to sea
617 level and energy budget not detectable over the past decade, *Nature Climate Change, 4*,
618 doi:10.1038/NCLIMATE2387.

619

620 Loeb, N. G., J. M. Lyman, G. C. Johnson, R. P. Allan, D. R. Doelling, T. Wong, B. J. Soden, and G.
621 L. Stephens (2012), Observed changes in top-of-atmosphere radiation and upper-ocean heating
622 consistent within uncertainty, *Nature Geoscience*, *5*, 110-113.

623

624 Loeb, N. G., H. Wang, A. Cheng, S. Kato, J. T. Fasullo, K. Xu, and R. P. Allan (2015),
625 Observational constraints on atmospheric and oceanic cross-equatorial heat transports: revisiting the
626 precipitation asymmetry problem in climate models, *Clim Dyn*, doi: 10.1007/s00382-015-2766-z.

627 Lucarini, V., and F. Ragone (2011), Energetics of climate models: net energy balance and meridional
628 enthalpy transport. *Rev. Geophys.*, *49*, RG1001, doi:10.1029/2009RG000323.

629 Lucarini, V., R. Blender, C. Herbert, F. Ragone, S. Pascale, and J. Wouters (2014), Mathematical

630 and physical ideas for climate science, *Rev. Geophys.*, *52,* 809–859, doi:10.1002/2013RG000446.

631

632 Lyman, J. M., and G. C. Johnson (2014), Estimating global ocean heat content changes in the upper
633 1800 m since 1950 and the influence of climatology choice, *Journal of Climate, 27*, 1946-1958,
634 doi:10.1175/ JCLI-D-12-00752.1.

635

636 Martínez-Garcia, A., A. Rosell-Melé, E. L. McClymont, R. Gersonde, and G. H. Haug (2010),
637 Subpolar Link to the Emergence of the Modern Equatorial Pacific Cold Tongue, *Science*, *328*, 1550-
638 1553, doi: 10.1126/science.1184480.

639

Mayer, M., and L. Haimberger (2012), Poleward Atmospheric Energy Transports and Their Variability as Evaluated from ECMWF Reanalysis Data, *J. Climate, 25*, 734–752, doi: http://dx.doi.org/10.1175/JCLI-D-11-00202.1.

Mayer, M., L. Haimberger, and M. A. Balmaseda (2014), On the Energy Exchange between Tropical Ocean Basins Related to ENSO, *J. Climate*, *27*, 6393–6403, doi: http://dx.doi.org/10.1175/JCLI-D-14-00123.1.

Mayer, M., K. E. Trenberth, L. Haimberger, and J. T. Fasullo (2013), The Response of Tropical Atmospheric Energy Budgets to ENSO, *Journal of Climate*, *26,* 4710-4724.

Meehl, G. A., J. M. Arblaster, J. T. Fasullo, A. Hu, and K. E. Trenberth (2011), Model-based evidence of deep-ocean heat uptake during surface-temperature hiatus periods, *Nat. Clim. Change*, *1*, 360–364.

Meehl, G. A., H. Teng, and J. M. Arblaster (2014), Climate model simulations of the observed early-2000s hiatus of global warming, *Nature Climate Change, 4*, doi: 10.1038/NCLIMATE2357.

Mizielinski, M. S., et al. (2014), High resolution global climate modelling; the upscale project, a large simulation campaign, *Geosci. Model Dev. Discuss.*, *7*, 563–591, doi:10.5194/gmdd-7-563-2014.

Morice, C. P., J. J. Kennedy, N. A. Rayner, and P. D. Jones (2012), Quantifying uncertainties in global and regional temperature change using an ensemble of observational estimates: The HadCRUT4 data set, *J. Geophys. Res., 117*, D08101, doi:10.1029/2011JD017187.

Moum, J. N., A. Perlin, J. D. Nash, and M. J. McPhaden (2013), Seasonal sea surface cooling in the equatorial Pacific cold tongue controlled by ocean mixing. *Nature*, *500*, 64-67, doi:10.1038/nature12363.

Otto, A. et al. (2013), Energy budget constraints on climate response, *Nature Geoscience, 6*, 415–416 doi:10.1038/ngeo1836.

Palmer, M. D., and D. J. McNeall (2014), Internal variability of Earth's energy budget simulated by CMIP5 climate models, *Environ. Res. Lett*. *9,* 034016, doi:10.1088/1748-9326/9/3/034016.

Poli, P., H. Hersbach, D. Tan, D. Dee, J.-N. Thépaut, A. Simmons, C. Peubey, P. Laloyaux, T. Komori, P. Berrisford, R. Dragani, Y. Trémolet, E. Holm, M. Bonavita, L. Isaksen, and M. Fisher (2013), The data assimilation system and initial performance evaluation of the ECMWF pilot reanalysis of the 20th-century assimilating surface observations only (ERA-20C), ECMWF Technical Report.

677 Liepert, B. G., and M. Previdi (2012), Inter-model variability and biases of the global water cycle in
678 CMIP3 coupled climate models, *Environ. Res. Lett. 7*, 014006, *doi:10.1088/1748-9326/7/1/014006.*

679

680 Raddatz et al. (2007), Will the tropical land biosphere dominate the climate-carbon cycle feedback
681 during the twenty first century? *Climate Dynamics, 29*, 565-574, doi 10.1007/s00382-007-0247-8,

682

683 Rienecker, M. M., M. J. Suarez, R. Gelaro, R. Todling, J. Bacmeister, E. Liu, M.G. Bosilovich, S.D.
684 Schubert, L. Takacs, G.-K. Kim, S. Bloom, J. Chen, D. Collins, A. Conaty, A. da Silva, et al.
685 (2011), MERRA: NASA's Modern-Era Retrospective Analysis for Research and Applications. *J.*
686 *Climate, 24*, 3624-3648, doi:10.1175/JCLI-D-11-00015.1.

687

688 Roemmich, D., J. Church, J.Gilson, D. Monselesan, P. Sutton, and S. Wijffels (2015), Unabated
689 planetary warming and its ocean structure since 2006, *Nature Climate Change, 5*, doi:
690 10.1038/NCLIMATE2513.

691

692 Rotstayn, L. D. M. A. Collier, M. R. Dix, Y. Feng, H. B. Gordon, S. P. O'Farrell, I. N. Smith, and J.
693 Syktusd (2010), Improved simulation of Australian climate and ENSO-related rainfall variability in a
694 global climate model with an interactive aerosol treatment, *Int. J. Climatol. 30*, 1067–1088, doi:
695 10.1002/joc.1952.

696

697 Sardeshmukh, P. D., and B. J. Hoskins (1984), Spatial smoothing on the sphere. *Mon. Weather Rev.*
698 *112*: 2524–2529.

699

700 Schmetz, J. (1991), Retrieval of surface radiation fluxes from satellite data, *Dynamics of*
701 *Atmospheres and Oceans, 16*, 61–72, doi: 10.1016/0377-0265(91)90012-5.

702

703 Schmidt, G. A., et al. (2014), Configuration and assessment of the GISS ModelE2 contributions to
704 the CMIP5 archive, *J. Adv. Model. Earth Syst.*, *6*, 141–184, doi:10.1002/2013MS000265.

705

706 Scoccimarro E., S. Gualdi, A. Bellucci, A. Sanna, P.G. Fogli, E. Manzini, M. Vichi, P. Oddo, and A.
707 Navarra (2011), Effects of Tropical Cyclones on Ocean Heat Transport in a High Resolution
708 Coupled General Circulation Model. *J. of Climate*, *24*, 4368-4384.

709

710 Simmons A. J., and D. M. Burridge (1981), An energy and angular-momentum conserving vertical
711 finite-difference scheme and hybrid vertical coordinates. *Mon. Weather Rev. 109*: 758–766.

712

713   Smith, D. M. , R. Allan, A. C. Coward, R. Eade, P. Hyder, C. Liu, N. G. Loeb, M. D. Palmer, C. D.
714   Roberts, , and A. A. Scaife (2015), Earth's energy imbalance since 1960 in observations and CMIP5
715   models, *Geophysical Research Letters,* doi: 10.1002/2014GL062669.

716

717   Stephens, G. L., J. Li, M. Wild, C. A. Clayson, N. Loeb, S. Kato, T. L'Ecuyer, P. W. Stackhouse Jr,

718   M. Lebsock, and T. Andrews (2012), An update on earth's energy balance in light of the latest

719   global observations. *Nature Geoscience*, 5, 691-696, doi:10.1038/ngeo1580.

720

721   Taylor, K. E., R. J. Stouffer, and G. A. Meehl (2012), An overview of CMIP5 and the experiment
722   design, *Bull. Am. Meteorol. Soc. 93,* 485–98.

723

724

725   Trenberth, K. E., and J. T. Fasullo (2013a), An apparent hiatus in global warming? *Earth's Future*,
726   doi: 10.002/2013EF000165.

727

728   Trenberth, K. E., and J. T. Fasullo (2013b), Regional energy and water cycles: Transports from
729   ocean to land. *J. Climate*, *26*, 7837-7851, doi:10.1175/JCLI-D-00008.1.

730

731   Trenberth, K. E., J. M. Caron, D. P. Stepaniak (2001), The atmospheric energy budget and
732   implications for surface fluxes and ocean heat transports. *Clim Dyn, 17,* 259-276.

733

734   Trenberth, K. E., J. T. Fasullo, and M. A. Balmaseda (2014), Earth's Energy Imbalance, *J. Climate,*
735   *27*, doi:10.1175/jcli-d-13-00294.1.

736

737   Trenberth, K. E., J. T. Fasullo, and J. Kiehl (2009), Earth's global energy budget, *Bull. Amer.*
738   *Meteor. Soc.*, *90*, 311-323.

739

740   Trenberth, K. E., and A. Solomon (1994), The global heat balance: heat transports in the atmosphere
741   and ocean, *Climate Dynamics*, *10*, 3, 107-134.

742

743   Voldoire, A., et al. (2012), The CNRM-CM5.1 global climate model: Description and basic
744   evaluation, *Clim. Dyn.*, *40*, 2091–2121, doi:10.1007/s00382-011-1259-y.

745

746   Volodin, E. M., N. A. Dianskii, and A. V. Gusev (2010), Simulating present-day climate with the
747   INMCM4.0 coupled model of the atmospheric and oceanic general circulations, *Izv. Atmos. Oceanic*
748   *Phys.*, *46*, 414–431, doi:10.1134/S000143381004002X.

749

750   Walters, D. N., et al. (2011), The Met Office Unified Model Global Atmosphere 3.0/3.1 and JULES
751   Global Land 3.0/3.1 configurations, *Geosci. Model Dev. Discuss.*, *4*, 1213–1271, doi:10.5194/gmdd-
752   4-1213-2011.

753

754   Watanabe, M., H. Shiogama, H. Tatebe, M. Hayashi, M. Ishii, and M. Kimoto (2014), Contribution
755   of natural decadal variability to global warming acceleration and hiatus, *Nature Climate Change, 4,*
756   doi: 10.1038/NCLIMATE2355.

757

758   Watanabe, S., T. Hajima, K. Sudo, T. Nagashima, T. Takemura, H. Okajima, T. Nozawa, H. Kawase,
759   M. Abe, T. Yokohata, T. Ise, H. Sato, E. Kato, K. Takata, S. Emori, and M. Kawamiya (2011),
760   MIROC-ESM 2010: model description and basic results of CMIP5-20c3m experiments, *Geosci.*
761   *Model Dev.*, *4*, 845-872, doi:10.5194/gmd-4-845-2011.

762

763   Wild, M., D. Folini, , M. Hakuba, C. Schär, S. I. Seneviratne, S. Kato, D. Rutan, C. Ammann, E.
764   F.Wood and G. König-Langlo (2015), The energy balance over land and oceans: An assessment
765   based on direct observations and CMIP5 climate models, *Clim. Dyn., 44*, doi:10.1007/s00382-014-
766   2430-z.

767

768   Wild M., D. Folini, C. Schar, N. Loeb, E. G. Dutton, and G. Konig-Langlo (2013), The global energy
769   balance from a surface perspective. *Clim. Dyn., 40,* 3107–3134, doi: 10.1007/s00382-012-1569-8.

770

771   Willett, C. S., R. R. Leben, and M. F. Lavın (2006), Eddies and tropical instability waves in the
772   eastern tropical Pacific: A review, *Progress in Oceanography, 69,* 218–238,
773   doi:10.1016/j.pocean.2006.03.010.

774

775   Wong, T., B. Wielicki, R. Lee, G. Smith, K. Bush, and J. Willis (2006), Reexamination of the
776   observed decadal variability of the Earth radiation budget using altitude-corrected ERBE/ERBS
777   nonscanner WFOV data, *J. Clim.*, *19*, 4028–4040, doi:10.1175/JCLI3838.1.

778

779   Yang, H., and K. K. Tung (1998), Water vapor, surface temperature, and the greenhouse effect—A
780   statistical analysis of tropical-mean data*, J. Clim., 11*, 2686–2697, doi:10.1175/1520-
781   0442(1998)011<2686:WVSTAT>2.0.CO;2.

782

783   Yukimoto, S., et al. (2012), A new global climate model of meteorological research institute: MRI-
784   CGCM3—Model description and basic performance*, J. Meteorol. Soc. Jpn.*, *90*, 23–64.

785

786   Zhang, Z. S., K. Nisancioglu, M. Bentsen, J. Tjiputra, I. Bethke, Q. Yan, B. Risebrobakken, C.
787   Andersson, and E. Jansen (2012), Pre-industrial and mid-Pliocene simulations with NorESM-L,
788   *Geosci. Model Dev. Discuss.*, *5*, 119–148, doi:10.5194/gmdd-5-119-2012.

789

790   **Figure captions**

791

792   **Fig. 1.** Schematic illustrating the energy flow terms used in the estimation of surface energy flux
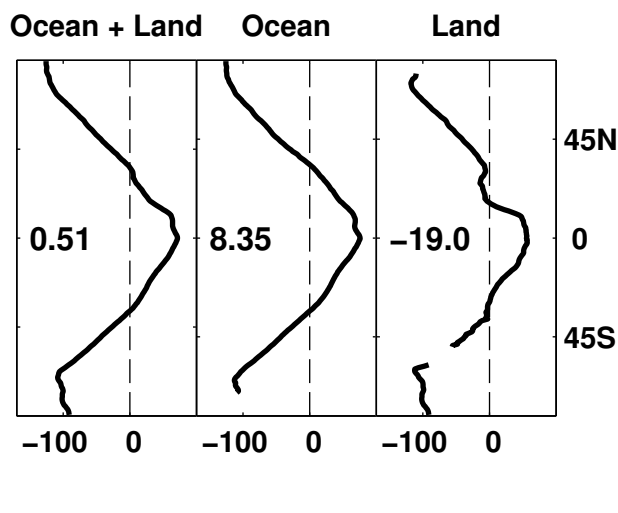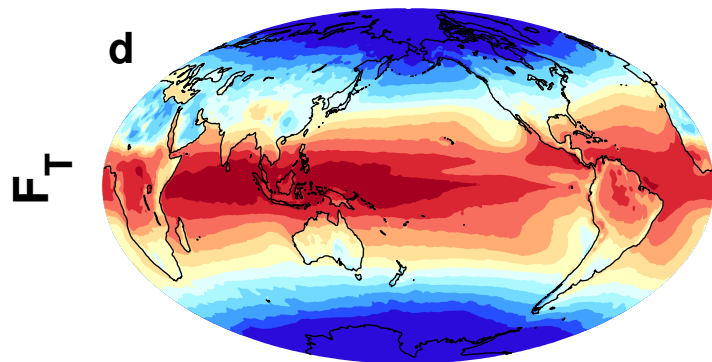793   over land and ocean.

794

795   **Fig. 2.** Deseasonalised anomaly (relative to the 2001-2005 period) time series of mean net downward
796   radiation fluxes at TOA over (a) the globe, (b) the global ocean and (c) the global land, for data sets
797   of AMIP5, ERAINT, WFOV, F_T and UPSCALE. Shaded areas of AMIP5 are sixteen member
798   ensemble mean ± 1 standard deviation. All lines are 6 month running mean. The WFOV anomaly
799   (60°S-60°N) is relative to 1985-1999 period, its line is three data points (three 72 day means) running
800   mean and is adjusted to match F_T. The y-axis unit is W/m^2 on the left and PW on the right. (d) is the
801   multi-annual (2001-2005) mean from F_T. The area mean (W/m^2) is displayed in the zonal mean plot.

802

803   **Fig. 3.** (a) Multi-annual (2001-2005) mean net downward energy fluxes (in W/m^2) at surface from
804   F_{mass}. Zonal mean variations from AMIP5, F_{mass}, F_{res}, ERAINT, ERA20C, UPSCALE and
805   $F_{mass-MERRA}$ are in the lower panel for (b) the globe, (c) the global ocean and (d) the global land,
806   respectively. Shaded areas of AMIP5 are sixteen member ensemble mean ±1 standard deviation. The
807   area mean is displayed in the zonal mean plot.

808

809   **Fig. 4**. (a) Multi-annual mean (2001-2005) northward total meridional energy transport (unit is PW)
810   calculated from E_{Dmass}, E_{Dres} and $E_{Dmass-MERRA}$; (b) multi-annual mean difference (2001-2008
811   minus 1986-2000).

812

813   **Fig. 5.** Multi-annual (2001-2005) mean net downward surface energy flux (in W/m^2) differences
814   between F_{mass} and (a) F_{res}, (b) ERAINT, (c) ERA20C, (d) $F_{mass-MERRA}$, (e) UPSCALE and (f)
815   AMIP5. The grid points of zero values are marked white and the RMS differences are given at the
816   top-right corner.

817

818

Fig. 6. Change in net energy fluxes (W/m^2, 2001-2008 minus 1986-2000) at TOA (left column), at surface (middle column) and the difference (right column) between fluxes at surface and TOA from reconstructions (F_{mass}, F_{res} and $F_{mass-MERRA}$), UPSCALE and AMIP5 data sets. a-c show the reconstruction based on *Allan et al.* [2014] at the TOA and the mass correction method using ERA Interim data, d-e are based on the residual method using ERA Interim data, f-g show the estimates from the mass correction method using MERRA reanalysis data, h-j are from the 5 ensemble mean of the UPSCALE simulations and k-m are the 16 ensemble member mean from the AMIP simulations. The marked area in b,d and f is from 20°N-20°S and 210°E to the west coast of central America.

Fig 7. Deseasonalised anomaly (relative to the 2001-2005 period) time series of mean net downward energy fluxes at surface over (a) the globe, (b) the global ocean and (c) the global land, from data sets of AMIP5, ERAINT, ERA20C, derived (F_{mass}, F_{res} and $F_{mass-MERRA}$) and UPSCALE. Light grey shadings denote the ± standard deviations of the sixteen AMIP5 simulations. All lines are 6 month running mean. The y-axis unit is W/m^2 on the left and PW on the right.

F_T　　　　　　　　　F_T

⇓　　　　　　　　　⇓

$$\boxed{\dfrac{\partial E}{\partial t}}\qquad\qquad\boxed{\dfrac{\partial E}{\partial t}}$$

⇐ $\boxed{\begin{array}{c}E_D\\ \textbf{Bias corrected}\end{array}}$ ⇒　　⇐ $\boxed{\begin{array}{c}E_D\\ \textbf{Bias corrected}\end{array}}$ ⇒

⇐ **Transport**

F_S　　　　　　　　　F_S

Constrained ⇓　　　　　⇓ **Calculated**
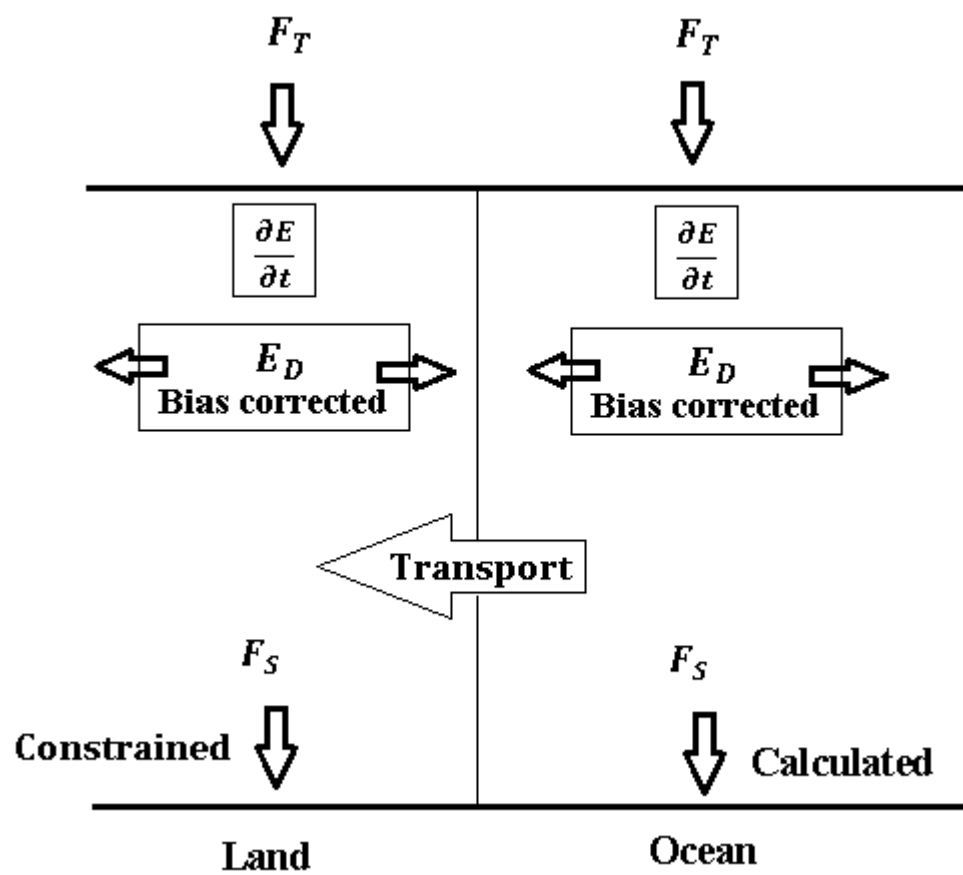
Land　　　　　　　　　Ocean

Net radiation flux anomaly at TOA

a — Ocean + Land (W/m², PW)

AMIP5
ERAINT
WFOV (60°S – 60°N)

b — Ocean

F_T
UPSCALE

c — Land

d — F_T — 2001–2005

Ocean + Land: 0.51

Ocean: 8.35

Land: −19.0

45N, 0, 45S

W/m²
−75 −45 −15 15 45 75

2001-2005

a

F_{mass}

b Ocean + Land

0.80
0.48
0.48
6.87
1.75
2.83
0.48

c Ocean

0.75
0.64
0.64
9.30
2.01
4.15
0.64

AMIP5
F_{mass}
F_{res}
ERAINT
ERA20C
UPSCALE
$F_{mass-MERRA}$

d Land

0.90
0.09
0.09
0.81
1.11
−0.68
0.09

Latitude

Zonal mean net surface flux (W/m^2)
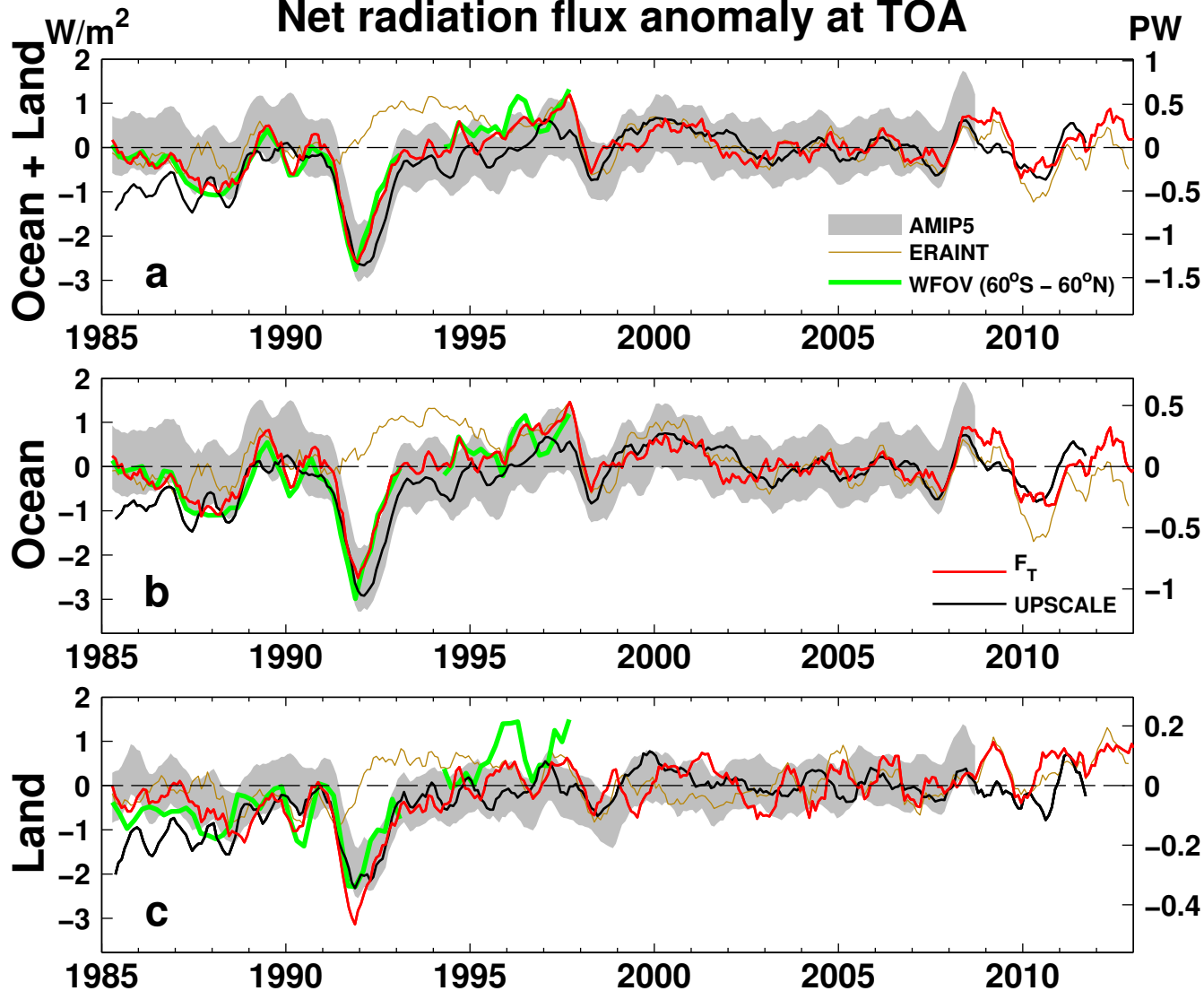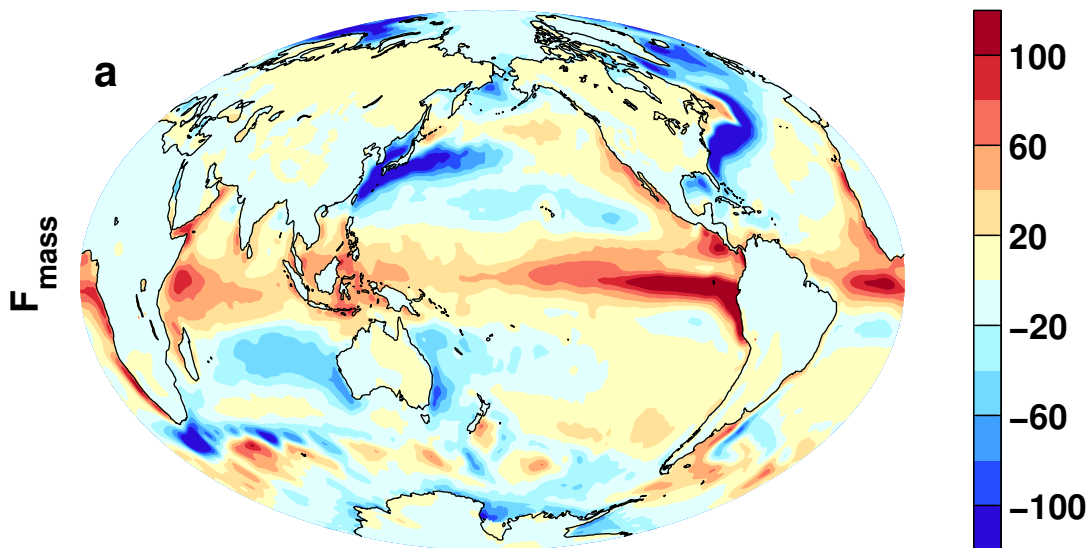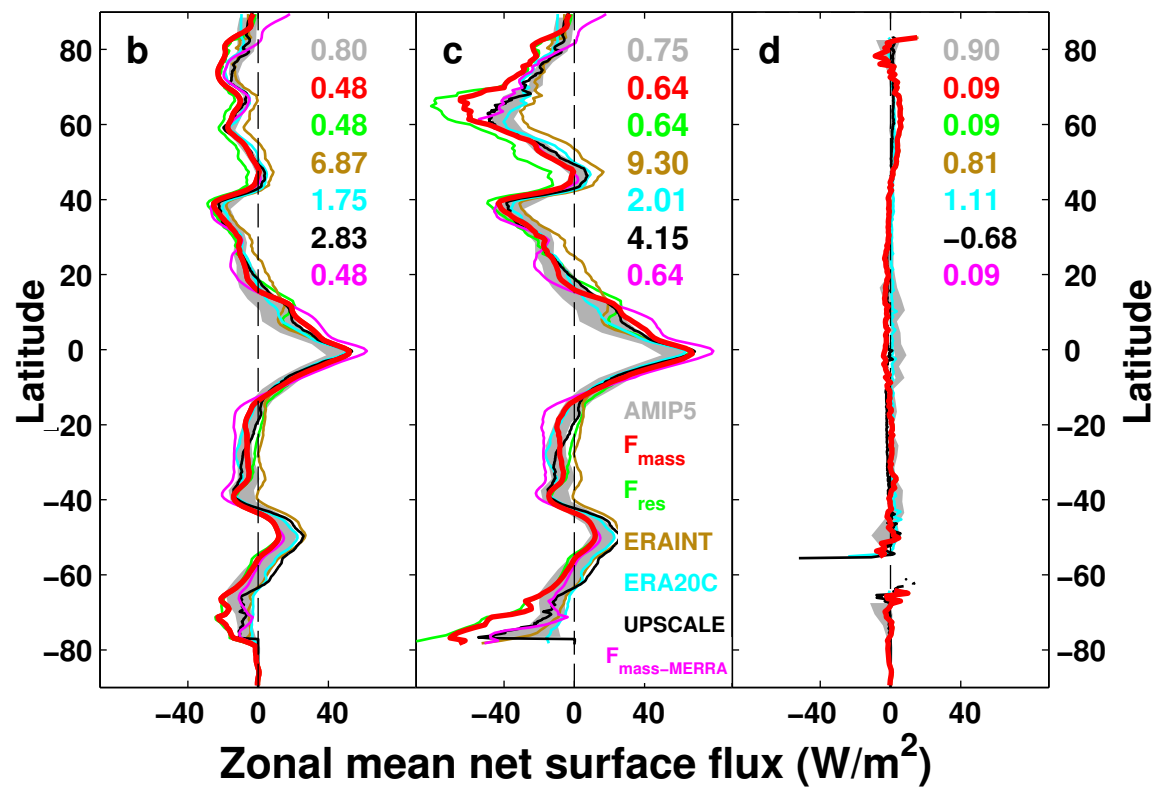
Northward total energy transport (PW)

a

from E_{Dmass}
from E_{Dres}
from $E_{Dmass-MERRA}$

Latitude
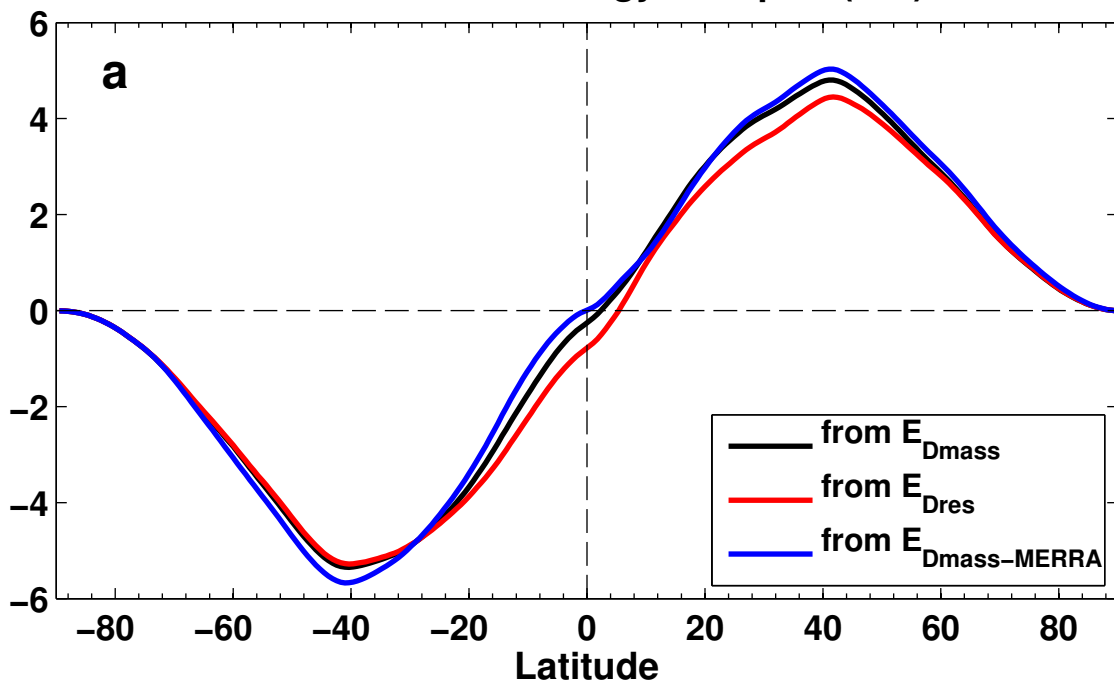
Difference (2001–2008 – 1986–2000) (PW)
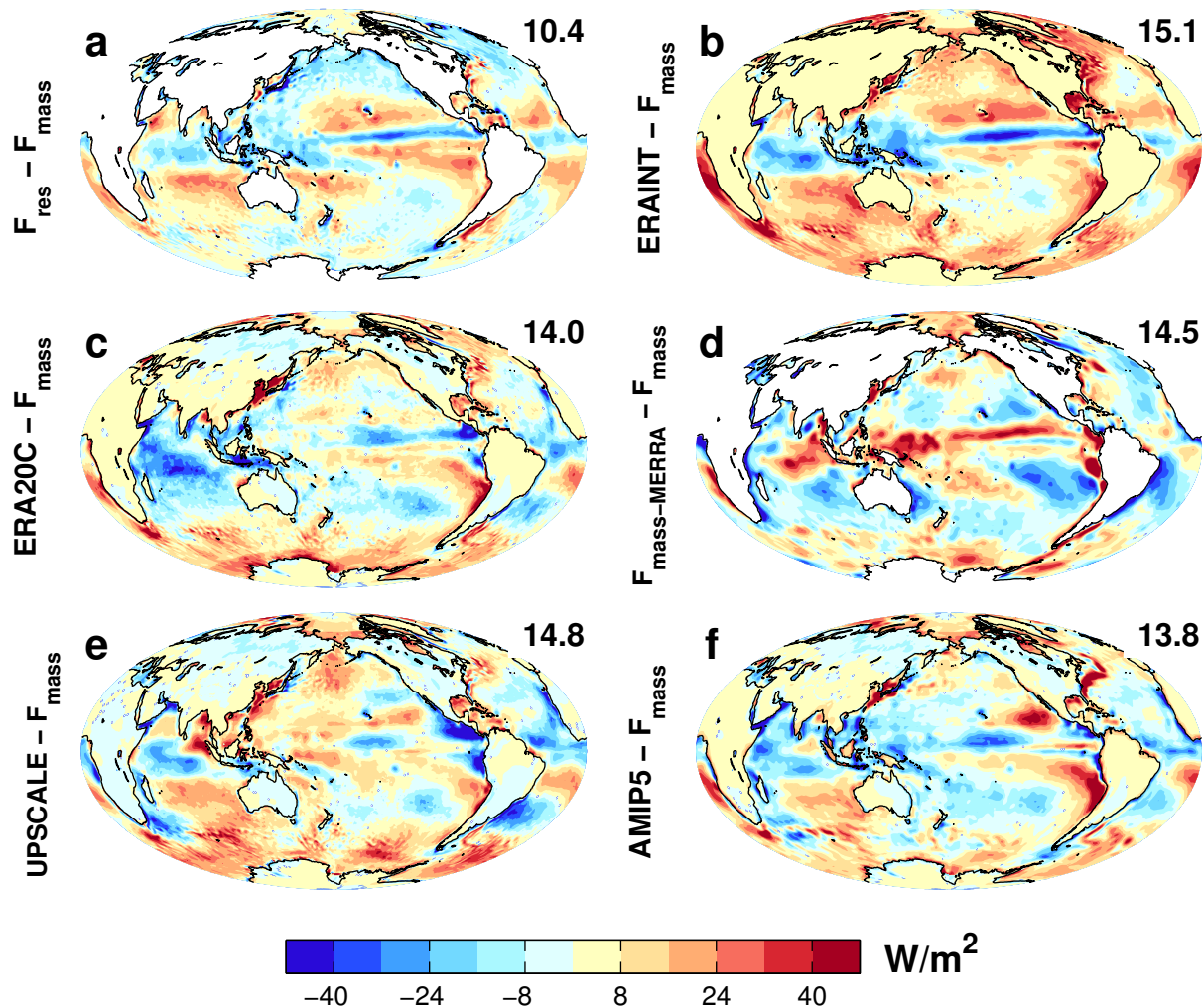
b

Latitude

2001−2005

2001–2008 – 1986–2000

Net downward energy flux anomaly at surface

a — Ocean + Land (W/m^2, PW)

Legend:
- AMIP5
- ERAINT
- ERA20C

b — Ocean (W/m^2, PW)

Legend:
- F_{mass}, F_{res}, $F_{mass-MERRA}$
- UPSCALE

c — Land (W/m^2, PW)

Year
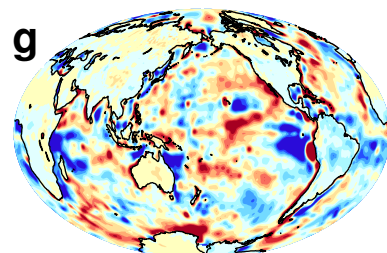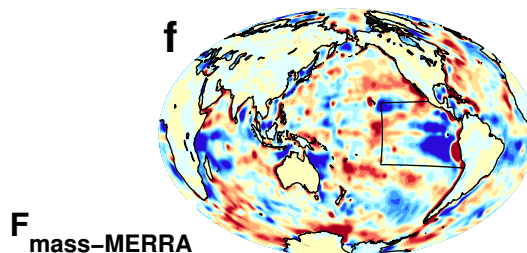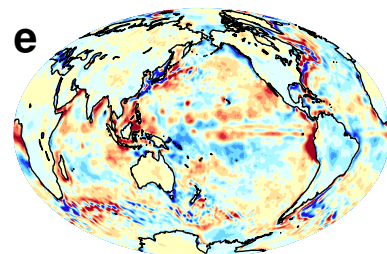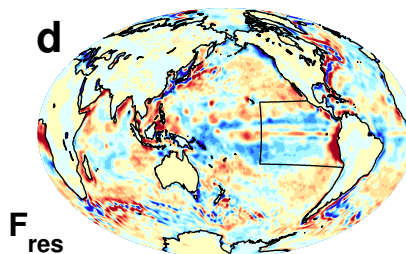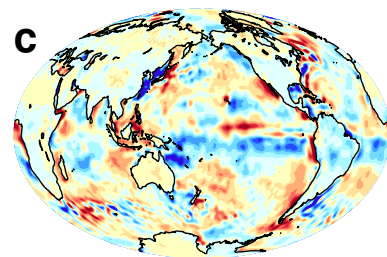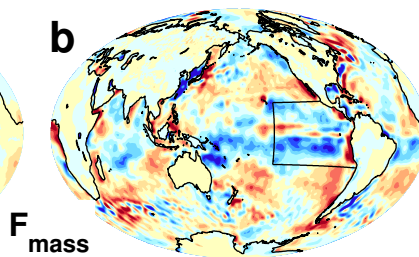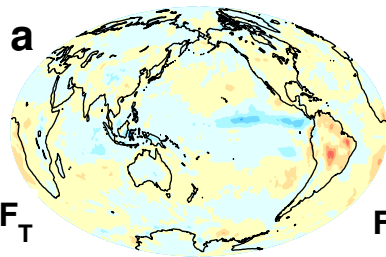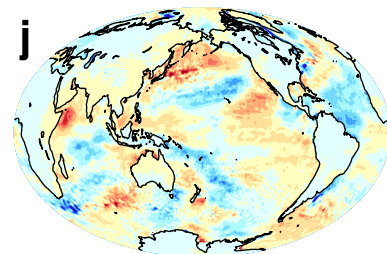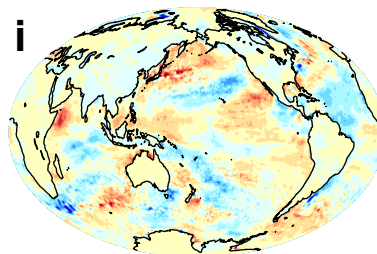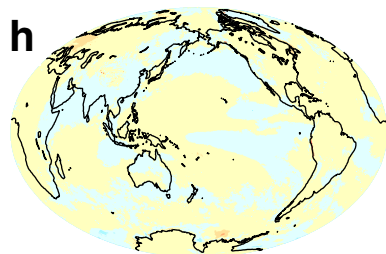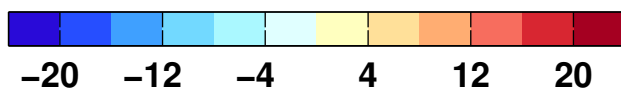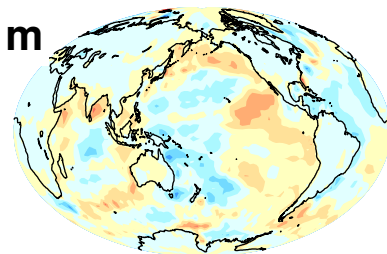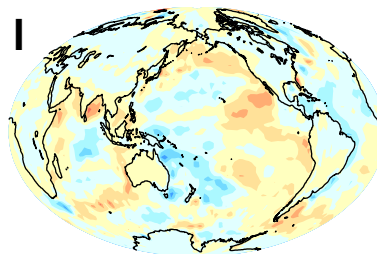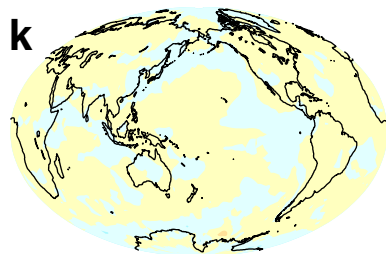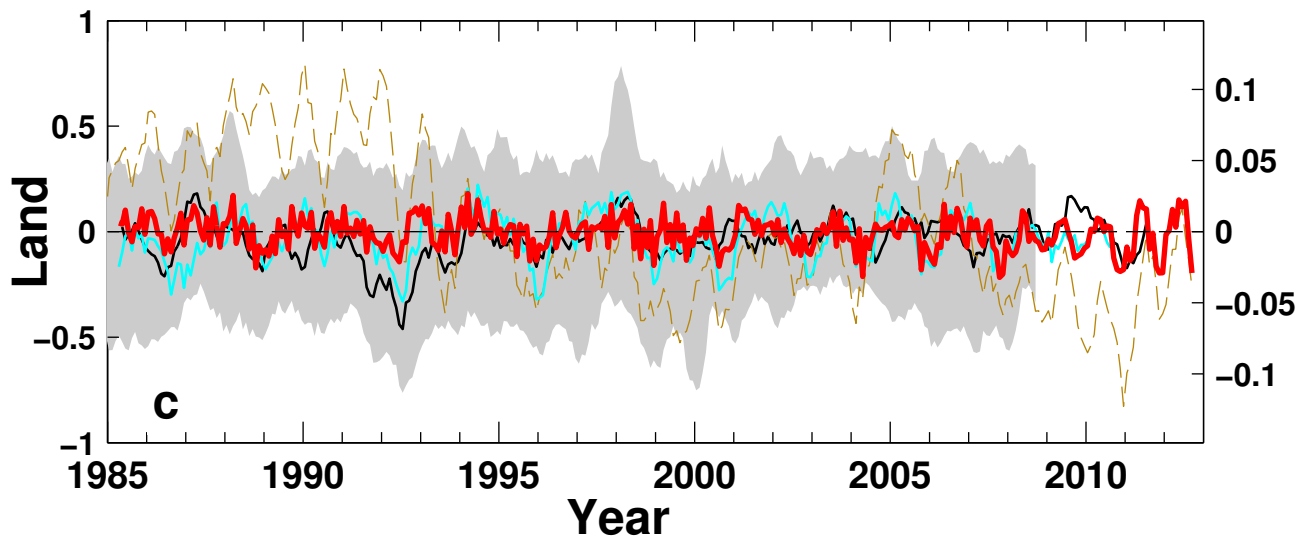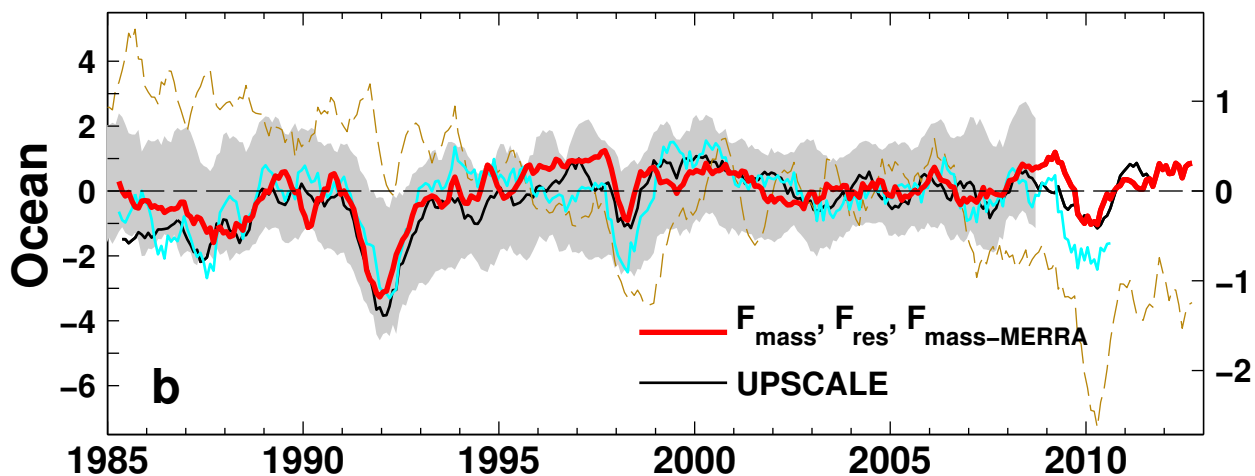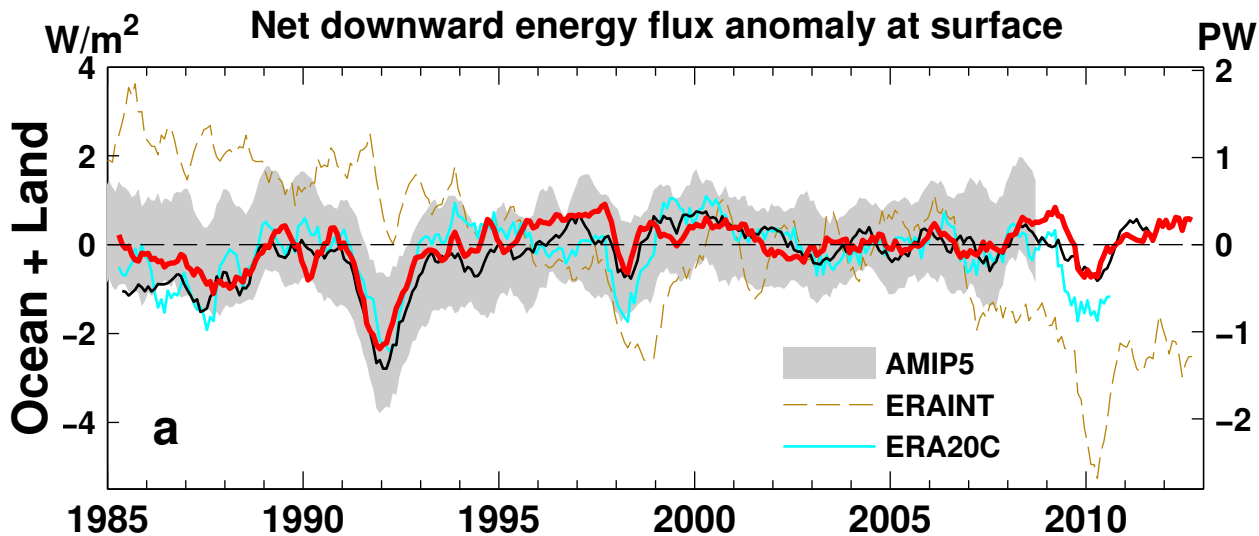
Table 1. Data sets and their properties

Data set	Period	Resolution (lat × lon)	References
CERES EBAF v2.8	2000-2012	$1.0^o \times 1.0^o$	*Loeb et al.* [2012]
Reconstruction	1985-2012	$1.0^o \times 1.0^o$	*Allan et al.* [2014]
ERA-Interim	1985-2012	$0.7^o \times 0.7^o$	*Dee et al.* [2011]
ERA20C	1985-2010	$0.7^o \times 0.7^o$	*Poli et al.* [2013]
MERRA	1985-2012	$0.5^o \times 0.7^o$	*Rienecker et al.* [2011]
HadCRUT4 v4.2.0.0	1985-2012	$5^o \times 5^o$	*Morice et al.* [2012]
AMIP5 models	1985-2008		
ACCESS1-0		$1.25^o \times 1.875^o$	*Bi et al.* [2013]
CanAM4		$2.79^o \times 2.81^o$	*Arora et al.* [2011]
CCSM4		$0.94^o \times 1.25^o$	*Gent et.al.* [2011]
CMCC-CM		$0.75^o \times 0.75^o$	*Scoccimarro et al.* [2011]
CNRM-CM5		$1.40^o \times 1.41^o$	*Voldoire et al.* [2012]
CSIRO-Mk3-6-0		$1.87^o \times 1.875^o$	*Rotstayn et al.* [2010]
FGOALS-s2		$1.66^o \times 2.81^o$	*Li et al.* [2013]
GFDL-CM3		$2.0^o \times 2.5^o$	*Delworth et al.* [2006]
GISS-E2-R		$2.0^o \times 2.5^o$	*Schmidt et al.* [2014]
HadGEM2-A		$1.25^o \times 1.875^o$	*Collins et al.* [2011]
INM-CM4		$1.5^o \times 2.0^o$	*Volodin et al.* [2010]
IPSL-CM5A-LR		$1.89^o \times 3.75^o$	*Dufresne et al.* [2013]
MIROC5		$1.39^o \times 1.41^o$	*Watanabe et al.* [2011]
MPI-ESM-LR		$1.85^o \times 1.875^o$	*Raddatz et al.* [2007)
MRI-CGCM3		$1.11^o \times 1.13^o$	*Yukimoto et al.* [2012]
NorESM1-M		$1.89^o \times 2.5^o$	*Zhang et al.* [2012]
UPSCALE	1985-2011	$0.35^o \times 0.23^o$	*Mizielinski et al.* [2014]